scientific reports

Check for updates

OPEN

A novel approach to double-strand DNA break analysis through γ-H2AX confocal image quantification and bio-dosimetry

Michael Valceski[1,2], Elette Engels[1,3], Sarah Vogel[1,2], Jason Paino[1], Dylan Potter[1,2], Carolyn Hollis[1,2], Abass Khochaiche[1,2], Micah Barnes[1], Matthew Cameron[3], Alice O'Keefe[1,2], Kiarn Roughley[1,2], Anatoly Rosenfeld[1], Michael Lerch[1], Stéphanie Corde[1,4] & Moeava Tehei[1,2]✉

DNA damage occurs in all living cells. γ-H2AX imaging by fluorescent microscopy is widely used across disciplines in the analysis of double-strand break (DSB) DNA damage. Here we demonstrate a method for the quantitative analysis of such DBSs. Ionising radiation, well known to induce DSBs, is used in this demonstration, and additional DBSs are induced if high-Z nanoparticles are present during irradiation. As a deliberate test of the methodology, cells are exposed to a spatially fractionated ionising radiation field, characterised by regions of high and low absorbed radiation dose that are only ever qualitatively verified biologically via γ-H2AX imaging. Here we validate our bio-dosimetric quantification method using γ-H2AX assays in the assessment of DSB enhancement. Our method reliably quantifies DSB enhancement in cells when exposed to either a spatially contiguous or fractionated irradiation fields. Using the γ-H2AX assay, we deduce the biological dose response, and for the first time, demonstrate equivalence to the independently measured physical absorbed dose. Using our novel method, we are also able quantify the nanoparticle DSB enhancement at the cellular level, which is not possible using physical dose measurement techniques. Our method therefore provides a new paradigm in γ-H2AX image quantification of DSBs, as well as an independently validated bio-dosimetry technique.

Keywords Confocal microscopy, Image analysis, Radiotherapy, Synchrotron, Microbeam Radiation Therapy, γH2AX, DNA damage, Double strand breaks, Dosimetry, Bio-dosimetry, Nanoparticles

DNA damage occurs in all cells, either as endogenous damage caused by the cell itself, or exogenous damage occurring in response to physical or chemical harms[1]. Radiation can cause physical damage through production of secondary radiation such as ionized electrons, and chemical damage through free radicals production, which can both produce genetic lesions. Chemotherapeutics, nanoparticles, and other drugs can also chemically induce such damage[2–5]. A primary lethal form of exogenous DNA damage is the double-strand DNA break (DSB), where both strands of the double-helix are severed within a short distance, often resulting in the death of the cell[6–9].

Detecting and measuring DSB induction is of broad interest in the scientific community across disciplines[1,10,11]. Many techniques have been utilised to detect DSBs, with amongst the most sensitive being the γH2AX immunofluorescent assay, which can detect DSBs at radiation doses as low as 1.2 mGy[10,11]. Fluorescent microscopy, flow cytometry and confocal microscopy have been used with γH2AX. In microscopy, DSB sites called foci are visible in images, which form following phosphorylation of H2AX molecules in response to DNA damage[1,11]. Whilst flow cytometry provides a statistical means of DSB quantification, it lacks the spatial information that microscopic imaging provides, which is important for any bio-dosimetric characterisation of radiation fields due to radiation-induced DNA damage[10]. Many authors have sought to link DSB induction to physical radiation dose in order to develop an accurate bio-dosimetric method[11–16].

[1]Centre for Medical Radiation Physics, University of Wollongong, Wollongong, NSW 2522, Australia. [2]Molecular Horizons, University of Wollongong, Wollongong, NSW 2522, Australia. [3]Australian Synchrotron - Australian Nuclear Science and Technology Organisation (ANSTO), 800 Blackburn Road, Clayton, VIC 3168, Australia. [4]Prince of Wales Hospital, Randwick, NSW 2031, Australia. ✉email: moeava@uow.edu.au

However, limitations exist in processing even high-resolution imaging. The conventional approach is to count resolvable foci, which are assumed to directly represent DSBs[1,10–12]. Standard methods utilise the mean pixel intensity of the foci, the number of foci per nucleus, or perform a qualitative or time-trial assessment of the foci[11,17]. However, some authors have observed that higher foci densities, and overlap between these, can result in the underestimation of DSBs, whilst others note that additional criteria such as foci size need to be considered[13,15,17–19].

Our approach to overcoming these limitations will be showcased in two challenging examples. High-Z nanoparticles (NPs) are known to enhance radiation dose to cancer cells and increase DNA damage[4,20–25]. Gold, gadolinium, tantalum- and thulium-based nanoparticles can locally enhance radiation doses from orthovoltage X-rays in 9 L gliosarcoma (9LGS) brain cancer cells[4,23,26–32]. Metal oxide NPs such as tantalum oxide and thulium oxide are shown to cluster around 9LGS cell nuclei and have estimated physical dose enhancements of at least 4 times the dose to water[31]. This localises significant DNA damage near nanoparticle aggregates and creates a unique and challenging case study for image quantification of the γH2AX foci density[4].

Microbeam Radiation Therapy (MRT) presents another challenge for DNA damage quantification due to vertiginous dose gradients. MRT uses highly collimated and high dose rate (HDR) synchrotron X-rays that are tens of microns wide and hundreds of microns apart to spare healthy tissue whilst delivering significant damage to malignant tumours[33–37]. In-beam, peak doses can be over hundreds of Gy, whilst the valley dose between microbeams are often < 20 Gy. The ratio between the peak and valley doses, known as the peak-to-valley dose ratio (PVDR), is used dosimetrically to define the MRT dose gradient[34,38]. MRT γH2AX foci quantification has been performed by counting foci per cell at different distances from peaks[39], taking advantage of the spatial information provided in imaging via microscopy techniques. However, despite the ability to quantify DSBs across peaks and valleys separately, a reliable biological confirmation of the physical PVDR has yet to be achieved and has been postulated to not be possible[40].

In this study, several radiation modalities are compared to assess the foci γH2AX expression and image quantification. We include DNA damage analysis of conventional broad-beam (CBB) orthovoltage X-rays, HDR synchrotron broad-beam (SBB), MRT, and when thulium oxide nanoparticles (TmNPs) are present. The fast delivery of synchrotron radiation at high dose rates (HDR) (typically > 40 Gy/s) has uniquely different effects compared with CBB[34,35,41–43]. This, in addition to the high dose gradients provided by MRT and with TmNPs, add an important dimension to the assessment of the reliability of γH2AX foci counting methods in conventional and non-conventional radiation fields.

We propose a new model to quantify DSB enhancement with γH2AX that can describe DNA damage in multiple irradiation conditions. This study will use the 9LGS cell model with and without TmNPs, and with CBB, SBB and MRT radiation modalities, to determine key parameters for the design of the model. Finally, we will validate a useable model for accurately verifying biological PVDR for MRT with γH2AX. We will demonstrate the flexibility of γH2AX imaging in verifying the cell response to physical collimation and dose delivery, thereby linking the biological response to physically prescribed dose for bio-dosimetry.

Results

A new framework to quantify γ-H2AX confocal images based on a foci factor

To overcome potential limitations of the γ-H2AX assay, including microscope resolution and foci overlap, a new model was developed to calculate DSBs when compared to a sample control. Figure 1 shows an overview of the sample preparation and image collection method, which was based on previous methods used[11], and the image analysis.

Following image acquisition and during the image analysis stage, we introduce a Foci Factor (FF) to account for variations in the number, size, and intensity of foci in any given cellular nucleus. The FF was developed for this study as a single metric to encapsulate the differences in foci across nuclei. The assumption is that the intensity of a single pixel is proportional to the number of DSBs present in that pixel, and this proportionality constant is consistent between images and pixels. Any foci of pixel value = 1 represents the same number of DSBs in any treatment. Therefore value 2 would represent twice the number of DSBs for another pixel, as would foci of two pixels of value = 1, and so on.

The total sum of all pixel values in all nuclear foci were counted to determine the FF. This accounted for any variations in foci size by area (larger foci represent more DSBs due to more pixels of some intensity value) or intensity representing density of DSBs in those foci.

$$FF = \frac{\sum_{i=1}^{n} RID_i}{c} \tag{1}$$

For Eq. 1, i is any given foci with a Raw Integrated Density (RID) value, n is the number of foci counted and c is the number of cells counted. The RID value (sum of all pixel values in an object or particle detected by ImageJ, i.e., a foci) was found from a particle analysis (Particle Analyzer tool) of thresholded γ-H2AX images on ImageJ (v1.53k)[44].

The full spectrum of particle area and mean pixel value (obtained from ImageJ analysis) was plotted to filter and gate the data to remove background noise, and discount 'false' foci and debris (Fig. 1e). Events were excluded below a minimum pixel value and area (40 and 0.2 μm^2 respectively for this study), as the area and pixel value had equivalent areas and intensities below these thresholds, indicating these events are particulates, image artifacts or noise, rather than substantial areas and intensities consistent with observed foci.

The number of DSBs per pixel value per pixel was assumed to be uniform across each image. Our model further supposes that DSBs are directly proportional to FF by the number of pixels. Only the proportionality of DSBs to the FF is required to determine DSB enhancement of a given treatment with respect to the control
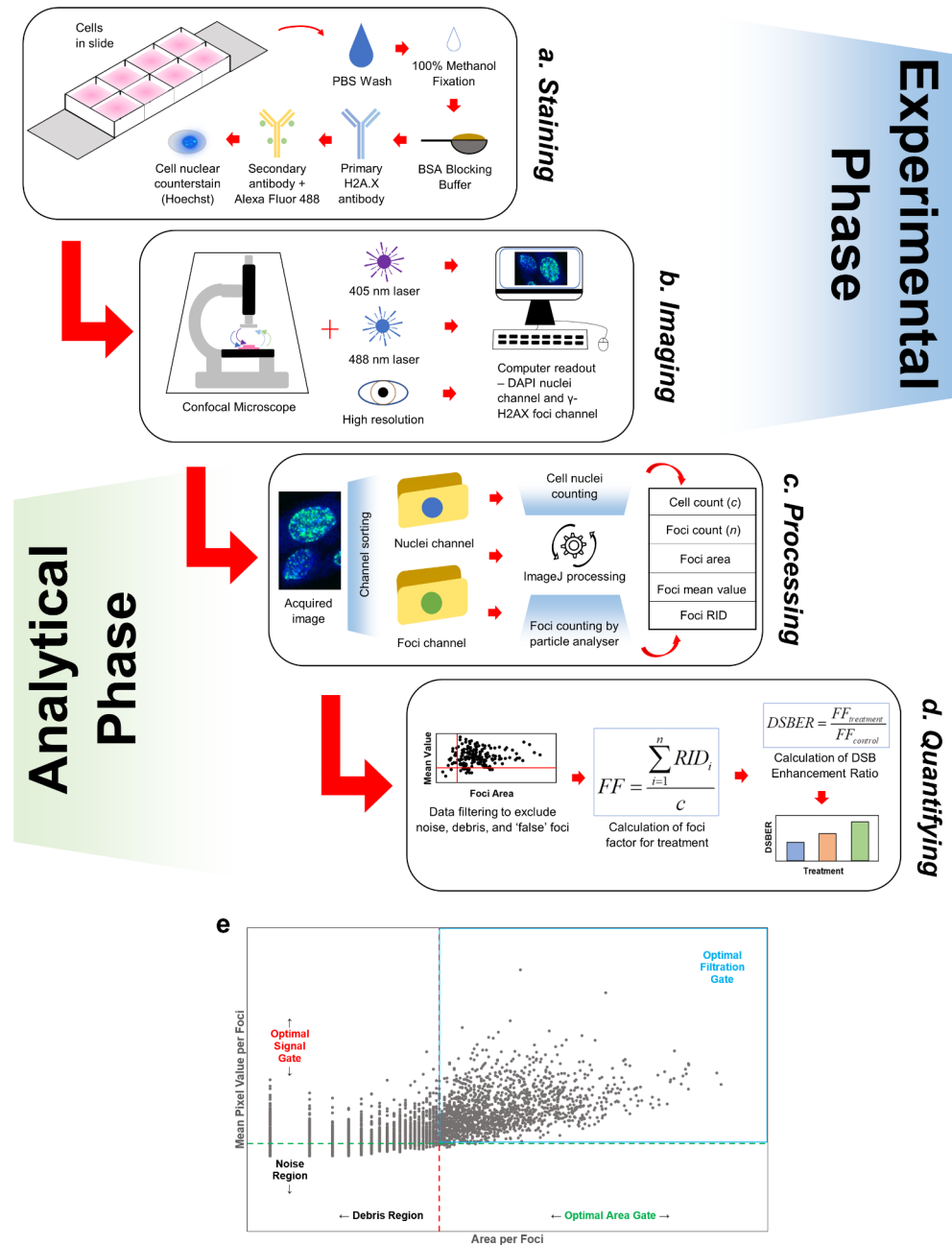
Fig. 1. Framework overview of Foci Factor Model methodology. Each stage of the FF method is displayed as a subfigure to demonstrate the experimental process and analysis methodology to quantify γ-H2AX images across a broad range of applications. (**a**), Staining of slides using a common method of γ-H2AX immunofluorescence staining[10,11]. (**b**), Stained cells imaged at 93x high-resolution at room temperature, using sequential channels for the 488 nm laser to fluoresce the Alex Fluor 488 conjugate labelled to the secondary antibody, and 405 nm laser to excite the Hoechst nuclear counterstain. (**c**), Acquired images sorted by channel and processed for analysis via ImageJ[44], whereby the number of cell nuclei are counted and the ImageJ particle analyser extracts the number, size and pixel intensity of each resolvable and overlapping foci. (**d**). Foci datasets filtered by area and mean pixel value to exclude background noise and debris, prior to the FF Model formulae were used for the final computation of FF and DSBER. (**e**). Detailed example (using 5 Gy conventional X-rays) of foci gating process in the Quantifying phase (**d**) using a scatter plot of foci mean pixel value (i.e., intensity) vs. foci area (μm) to filter data to exclude noise and debris from the count.

(untreated sample). This is presented as the DSB Enhancement Ratio (DSBER), determined as the ratio of foci factors of a treatment sample to the untreated (0 Gy) control, (Eq. 2).

$$\frac{FF_{treatment}}{FF_{control}} = \frac{DSB_{treatment}}{DSB_{control}} = DSBER \qquad (2)$$

The DSBER value was found for each radiation treatment condition using Eq. 2 during imaging analysis. In the next sections, the established methods of average number of foci per cell, average foci area, and average foci intensity were compared with DSBER for several varying conditions in cells to demonstrate the improvements of this proposed model.

Foci factors resolve quantification limits caused by high foci density and overlap

The FF method was compared under different irradiation conditions including conventional (CBB), high dose rate synchrotron radiation (SBB), MRT, and when TmNPs were present. Conventional methods of foci image analysis were compared with the FF model under the same conditions to asses our model for DNA damage quantification in complex radiation fields. Variations in DSB enhancement, including foci intensity, area, and number, are illustrated in Fig. 2. Analysis of the γH2AX images for each irradiation condition displayed in Fig. 2a are summarised in Fig. 2c-h.

Initially we will consider the expression of DNA damage in the presence of TmNPs in each method. Figure 2d demonstrates the standard foci/cell average for 5 Gy CBB shows very little difference between DSB induction in TmNPs compared with radiation only (within a significant error margin), despite the visual increase in γH2AX foci (Fig. 2a, b) and previous results in other studies when higher radiation doses are used[4]. Mean intensity has been observed to have some linear dependence on dose, but may saturate at higher doses[17]. Accordingly in this work, the mean intensity (throughout the population) of any given foci (but not pixel) shows saturation and no significant change with treatment (Fig. 2g). This is despite Fig. 2b showing more DSB induction through the abundance of foci generated near TmNPs clusters around the nuclei of 9LGS cells.

Foci area is not accounted for in the intensity or foci number methods. The dependence of radiation absorbed dose on foci area has previously been observed to follow a linear trend with γ-rays, and different radiation types have produced differences in foci size[14,17]. The FF method is able to account for foci area, and we show this method reduced the margin of error in DSBER for TmNPs samples compared with the foci/cell method alone; which may be due to foci overlap causing more variation in foci counting across images. Slight increases are seen with TmNPs present with radiation, yet these are not statistically significant, although still more significant than the non-significant differences observed in foci/cell and pixel intensity (Fig. 2d, g).

However, the foci area, RID and integrated density criteria also all consider foci size, and are the only quantification methods to demonstrate statistical significance in their results by doing so (Fig. 2e, f,h). They demonstrate not only larger foci, but also indicate a greater density of DSBs per foci (as larger foci have more pixels, so correlating to more DSBs). Foci/cell and intensity methods alone do not account for these and can underestimate DSB damage due to lack of separation[13,19]. Only the FF method, by combining these factors into a single parameter, can produce a reliable DSBER value. A 5 Gy dose of CBB X-rays induces 15.5 times more DSBs in 9LGS cells than 0 Gy controls (no treatment) using the FF method. With the addition of TmNPs during irradiation, the resulting DSBER increased two-fold, despite non-significant changes in DSB induction for 0 Gy. A DSB enhancement due to TmNPs was expected from a previous study (Engels et al. 2018), using clonogenic assay[4].

Now we will consider foci saturation in complex radiation fields. SBB has been shown to significantly decrease 9LGS survival with clonogenic assay beyond CBB (as observed previously by Engels et al.)[27,33]. We therefore expect significant DSB markers to be present. While SBB tended to increase foci/cell, foci area, and RID in our results, the significance was not captured by these methods alone. Only DSBER via the FF method produced a notable difference between SBB and CBB. MRT demonstrates significant DNA damage concentrated in the peak, despite significant foci overlap (Fig. 2a-c). Despite studies finding difficulty in counting foci in these conditions[19,40], only the FF method successfully accounts for this saturation and yields reliable results.

The increase in DSBER is highly significant in Fig. 2c and is clearly reflective of the overwhelming damage delivered by the to the peak (Fig. 2a, b). This indicated significant 9LGS cell killing with MRT due to such high damage overwhelming the DNA repair processes[8,45,46]. The FF method demonstrates this with a DSBER of 87.4 times more DSBs for radiation-only, correlating with previous work that observed a reduction in clonogenic survival for the same microbeam collimation[33]. Figure 2a also showed significant foci saturation in cells caught in and around MRT peaks (Fig. 2b), which the conventional foci/cell method cannot account for. This resulted in less foci/cell in MRT compared with SBB or even CBB (Fig. 2d) despite visual confirmation to the contrary (Fig. 2a), highlighting a limitation of the conventional method. Only by accounting for area can a reliable result be obtained by considering the significant differences in foci area with MRT (Fig. 2b, c,e, f,h), which is successfully determined via the FF method.

The FF method, focusing on RID per cell (Eq. 1), accounts for both pixel intensity and foci area, and therefore the severity, density, and spread, of DSBs in any given foci, even in cases with overwhelming DSBs (Fig. 2b). DSBER results in Fig. 2c better represents observable DSBs in the images in Fig. 2a and correlate with the expected increase in DSBs for CBB X-rays, further increasing when TmNPs are present[4]. It then becomes important to consider foci area, which significantly increases with MRT as well ($p < 0.00001$), to account for the larger, merged foci found in peaks. This demonstrates the flexibility of this method in overcoming existing analysis limitations.
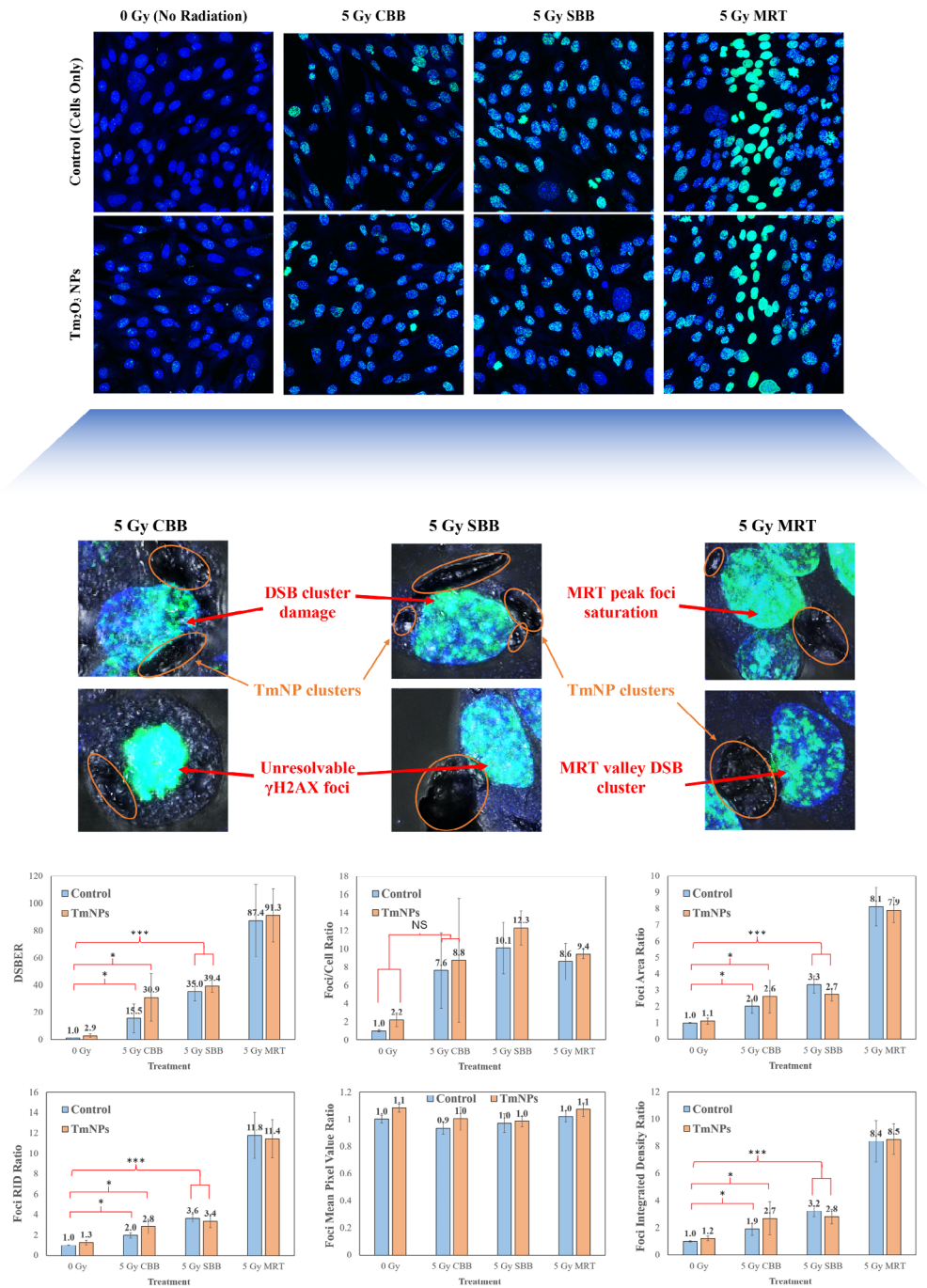
Fig. 2. Foci Factor Model improves quantification of DSBs when foci are difficult to resolve. (**a**), Panel of 9LGS confocal images quantified for each condition (maximum projections of a 10-slice Z-stack at 93x resolution) and showing γH2AX foci (green) overlayed on Hoechst nuclear-stained 9LGS cells nuclei (blue). (**b**), Image panel highlighting the effect of internalised TmNPs (orange circles) and MRT peaks on oversaturation of foci in images (**a**), resulting in visually overlapping foci clusters (red arrows) due to greater area rather than resolvable individual foci. (**c**), DSBER values calculated for each image in the panel (**a**), averaged from results from at least six replicate images (blue columns represent radiation-only, orange represent radiation combined with TmNPs). (**d-h**), Comparison of the conventional foci per cell counting method (**d**) with average foci area (**e**), average raw integrated density (RID) (**f**), foci mean pixel intensity (**g**), average foci integrated density (foci area multiplied by mean intensity) (**h**). All foci parameters are normalised to the respective 0 Gy (no NPs) controls to create the enhancement ratio. Red braces represent statistical significance following a student's unpaired one-tailed t-test, where NS = not significant, (*) = $p < 0.1$, (**) = $p < 0.05$, and (***) = $p < 0.01$. All data points displayed in this figure represent the average of at least six quantified images across independent experimental trials ($n = 6$) and display error bars representing standard error of the mean (SEM). Each sample imaged was fixed at 20 min post-irradiation.

Bio-dosimetric analysis of MRT using high-resolution confocal microscopy

To further validate the FF method, DSBER values were obtained for MRT fields at different doses to quantify the distinct DNA damage of the peaks and valleys for bio-dosimetry. Figure 3 demonstrates the importance of using a high-resolution imaging (93x for this study) modality such as a confocal microscope to obtain images of sufficient quality to confirm bio-dosimetric equivalence. This permitted a bio-dosimetric verification of the
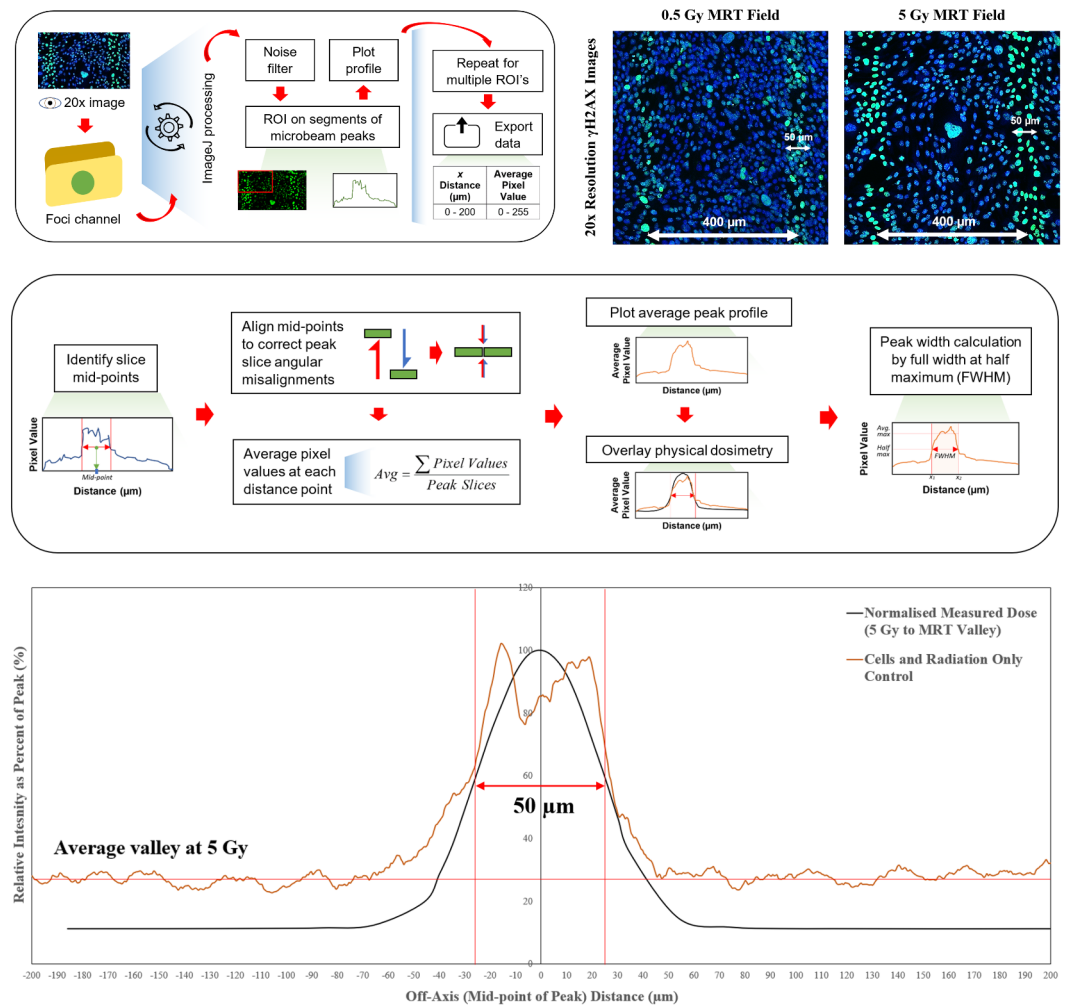

Fig. 3. High resolution confocal microscopy is effective in confirming a bio-dosimetric match between physical dose and biological response. (**a**), 20x γH2AX images expressing DSB foci (green) overlayed on Hoechst nuclear stains (blue) to show the biological response of the 9LGS cells to MRT microbeam arrays with 0.5 Gy and 5 Gy valleys observable by confocal microscopy. 20x resolution was chosen to capture multiple peaks in one image. Each image was acquired followed the method outlined in Fig. 1 a-b. The microbeam peaks of the physical MRT collimation align with the biological tracks expressed in DSBs in the γH2AX images at 20x dry resolution, with an observable match in both the width (50 μm) and pitch (400 μm) of the fields. (**b-c**), Method overview of the analytical image processing to extract and export peak profile data from 20x images, and subsequent analysis and correction process to form the average biological peak profile of a single microbeam (**d**). Regions of interest (ROI's) are drawn around slices of visible microbeam peaks to extract intensity data collapsed into 1D as a peak profile along the width of the ROI (**b**). Peak slice mid-points are identified to align peak mid-points across replicate ROI slices to correct for angular misalignment and cell movements before averaging data at each off-axis distance. A full width at half-maximum (FWHM) value can then be obtained as a measure of peak width (**c**). (**d**), Normalised measured dose (physical) profile of a single MRT peak (measured incrementally across the 400 μm pitch) compared with the biological response expressed in γH2AX foci intensity (mean pixel values averaged along y-axis in images using ImageJ[44]) in 9LGS cells, both with a 5 Gy MRT valley. Both peak profiles are normalised to their respective peak maximums for effective comparison (dose is normalised to maximum at peak centre, whilst the foci intensities are normalised to the average peak maximum across a 50 μm width centred on the peak). All data points displayed in this figure represent the average of at least six quantified images across independent experimental trials (n = 6) and display error bars representing standard error of the mean (SEM). Each sample imaged was fixed at 20 min post-irradiation.

biological response to the physical radiation dose delivered and confirmed the 9LGS cell damage reflected the expected physical collimation of the MRT field.

Figure 3 reveals that the DNA damage in the 9LGS cell population is varied spatially, and is well aligned to the physical dose regions defined by the dimensions of the MRT field (as indicated by the white arrows in Fig. 3a). The 20x images show bright and dense γH2AX fluorescence regions separated by 400 μm and 50 μm wide in accordance with the collimation (FWHM is (50.6 ± 7.3) μm for 0.5 Gy and (52.1 ± 2.5) μm for 5 Gy). Higher doses in the peak result in tracks of greater DNA damages (Fig. 3a). An observable roll-off in the transition zones[38] around the peak edges and into the near-beam regions of the valleys is also seen (Fig. 3a, d). The γH2AX images clearly follow these trends, demonstrating the biological response of 9LGS follows the expected physical delivery.

In Fig. 3b, c, by taking the available pixel intensity data across images such as those shown in Fig. 3a and collapsing these into 1D peak profiles across the x-axis of each image, and then expressing y-axis values as intensity allows for the development of biological profiles of the beam (Fig. 3d). The quality of confocal images taken and the γH2AX assay's sensitivity is sufficient to show a match between the biological FWHM in Fig. 3d and physical dose FWHM of the microbeam peaks. Again, the physical valley responses are relatively uniform beyond the transition zones, similar to the observed average biological response to the valley dose with γH2AX intensity.

However, the physical dose in the valleys is only half of the biological DNA damage. Although the raw intensity values of the γH2AX assay images provide a good indication of the distinct dose regions of MRT, quantifying the DNA damage, and relating this parameter to the physical dose was not possible due to non-linearity of the fluorescence intensity with dose. This is due to foci response, including intensity, being unable to distinguish between direct radiation damage and additional biological effects. Indirect and chemical damages such as free radicals, scatter and roll-off of peak dose into valleys, and later biological cell responses may all increase the DSB intensity observed in MRT valleys. This may be negligible compared to the overwhelmingly damaged peaks, resulting in comparatively greater valley damage and so reduced PVDR.

Indeed, if the average intensity of peak centre and the average of valley cells is used to calculate a biological measure of PVDR, a value of (3.2 ± 0.5) is obtained, which does not agree with the physical PVDR of 8.9 measured by radiation detectors. Additionally, the intensity detection via ImageJ across the image, which is a 2D maximum projection of all z-stack slices superimposed, averaged all pixel values along the y-axis for each increment along the x-axis. This does not account for the spaces between cells that did not have foci, and so inadvertently reduced the peak damage intensity and hence PVDR. These factors highlight the limitations of using γH2AX image intensity alone for bio-dosimetry, especially as only cellular foci and not spacings between cells should be considered. Instead, a breakdown of DSBER in peaks and valleys separately using the FF Model, which accounts only for foci and does so in 3D across the z-stack, can be used more effectively, as demonstrated in Fig. 4.

Foci factors validate bio-dosimetric properties of spatially fractionated microbeams

Figure 4 demonstrates the dependence of γH2AX DSB quantification on the analysis method used. The foci size, and the sum of intensity values in individual foci (the RID), are again the dominant factors alongside foci/cell in determining DSBER for MRT. Following a breakdown of peaks and valleys (Fig. 4a), the DSBER value for 4.45 Gy peaks (0.5 Gy valleys) is found to be close to the value for 5 Gy CBB, indicating that comparable doses deliver similar DNA damage. This follows from observations that foci induction and number, and foci size, have a dependence on absorbed dose[17,18], an effect seen in Fig. 4e, where significant increases in foci area are observed for 4.45 Gy MRT peaks that directly match the increases seen in 5 Gy CBB in Fig. 2. This further adds merit to the FF Model as it incorporates the role of foci area in the DSBER calculation. The close agreement of the 4.45 Gy MRT peak and 5 Gy CBB also occurs despite significant differences in dose rate. Figure 2 indicated that high dose rate SBB X-rays increased DSB induction compared to low dose rate X-rays, an effect also seen in literature with neutrons[18]. However, the valley dose is much lower and perhaps more comparable to the CBB irradiation for 9LGS cells.

However, DSB enhancement is lacking in the MRT fields with 5 Gy in the valley (44.5 Gy in the peak). The images in Fig. 4b show overwhelming DNA damage at these doses, suggesting there is saturation of resolvable DSBs in 9LGS, rendering any additional DNA damage as negligible or unquantifiable. Saturation of foci in MRT peaks has previously been observed in γH2AX imaging[39,40]. The FF method produced a higher DSBER in the peak than the valley compared to other methods, in response to the combination of foci area, number and intensity in the calculation. Thus, it includes effects of the MRT peak irradiation that respond to spatially clustered DNA damage (foci area, integrated dose), and overcomes the shortcoming of the traditional foci/cell and intensity methods, which showed no change in average DNA damage (Fig. 4g).

In particular, the foci/cell method in Fig. 4d shows confounding results for cells in the peak. The high density of foci overwhelmed the foci/cell counting model due to foci overlapping, producing low foci numbers in response. In contrast the valley showed more distinct foci and the foci/cell model computed higher numbers. This underestimation of DSBs in the peak exposes the major limitation of manual or even automatic foci counting methods[19]. Instead, the foci area increases significantly in the peak compared to the valley in Fig. 4e. This highlights the flexibility of the FF method in accounting for the case where individual foci are too large or overlap.

The sensitivity of γH2AX assay is high, and so quantification of foci as markers for DNA damage can be made using their intensity also. However, foci intensity alone in Fig. 4 was not sufficient to show the distinct DNA damage in the peak and valley. The RID, however, sums the total intensity across all pixels in the foci[44], and therefore integrates all intensity changes to account for both variations in pixel intensity in a foci, and overall
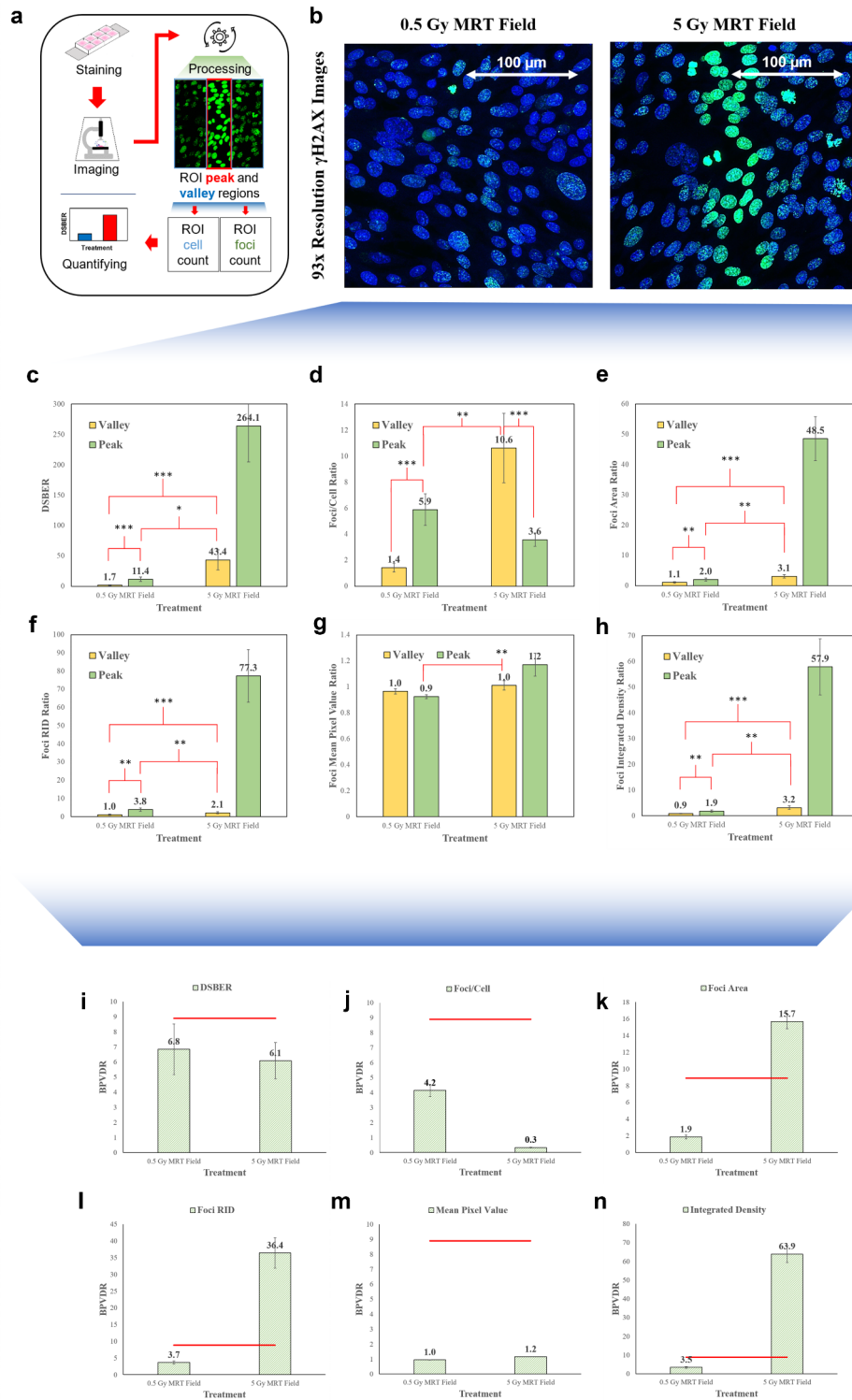
foci size. Accordingly, increases in foci area are proportional to increases in RID (and integrated density) seen in Figs. 2 and 4.

Additionally, the 5 Gy MRT valley DSBER values in Fig. 4c can be compared to the 5 Gy SBB results in Fig. 2c. It can be noted that the DSB induction in MRT valleys are very similar to (and well within experimental error of) values observed with SBB X-rays at the same dose, including changes in foci per area. This again demonstrates the dose dependence of foci and DSBs and allows this to be used as a reference to confirm DSB induction at 5 Gy in MRT valleys is accurate using the FF method, given the physical dose deposition is uniformly 5 Gy in MRT valleys (Fig. 3) and SBB fields.

Likewise, the peak values are well within error of 8.9 times the DSBER of 5 Gy SBB, proportional to the expected increase in dose with physical PVDR (measured as 8.9). As the FF Model has demonstrated that it can overcome many of the shortcomings of other models, it was then used to evaluate the biological PVDR (BPVDR)

◄**Fig. 4.** Foci Factors permit a reliable bio-dosimetric and spatial analysis of MRT field components. (**a**), Method overview for MRT DSB spatial analysis following the framework displayed in Fig. 1 and adjusting for individual MRT peak and valley analyses. Following staining and imaging of samples, this processing method requires the additional step of drawing regions of interest (ROI's) over peaks and their accompanying valleys. The same analysis steps in Fig. 1 can then be used for peaks and valleys separately to obtain DSBER via the FF Model for each part of the MRT field. (**b**), Sample 93x γH2AX images of MRT fields showing DSB foci (green) overlayed on Hoechst nuclear stains (blue) with 0.5 Gy and 5 Gy valleys, each centred on a single MRT microbeam. White arrows from each peak centre extending out into nearby valley indicate the scale of the image. Each image was acquired following the method shown in Fig. 1. (**c-h**), Enhancement ratio graphs demonstrating a bio-dosimetric quantification of DSB enhancement of MRT peak vs. valley regions of interest for the γH2AX images using the spatial information provided by high resolution confocal microscopy for 0.5 Gy and 5 Gy MRT valleys. Each values takes an average of results across at least six images. Each graph demonstrates the effectiveness of a different foci quantification method, including DSBER proposed in this study (**c**), foci per cell (**d**), average foci area (**e**), average foci RID (**f**), average foci mean pixel value (**g**) and average foci integrated density (area times mean value) (**h**). Red braces represent statistical significance following a student's unpaired two-tailed t-test, where (*) = p < 0.1, (**) = p < 0.05, and (***) = p < 0.01. Note all results in (b-f) and (h) are statistically significant compared to the untreated control in Fig. 2 (p < 0.05 for each), except the 0.5 Gy MRT valley in (**b**) and the 5 Gy MRT peak in c (not significant). (**i-n**), Biological PVDR (BPVDR) graphs expressed as the ratio of the peak DSB quantified values found for each method respectively (**c-h**) over the corresponding valley. The PVDR is determined as the ratio of the average peak enhancement to the average valley enhancement ratio for each of the six quantification methods. A red line on each graph indicates the physical PVDR of 8.9, as physically measured by radiation detectors. All data points displayed in this figure represent the average of at least six quantified images across independent experimental trials (n = 6) and display error bars representing standard error of the mean (SEM). Each sample imaged was fixed at 20 min post-irradiation.

in Figs. 4 and 5. This was done by taking the ratio of the FF value for the peak with the FF for the combined valleys. Equation 3 calculates BPVDR from the MRT images to confirm it matches physical PVDR. This allows for a comparison of the average BPVDR values for all replicate images of a given sample, for both MRT doses. These results are shown in Fig. 4i-n and Fig. 5d-i for all methods assessed.

$$BPVDR = \frac{FF_{peak}}{FF_{valley}} \tag{3}$$

Only the FF method yields a value close to expected 8.9 physical PVDR value measured. Figure 4j demonstrates that 5 Gy MRT fields have a BPVDR less than 1 and lower than the corresponding 0.5 Gy field. This is due to foci saturation reducing foci/cell in high dose peaks (Fig. 4d) to lower than valleys despite the expected converse observed (Fig. 4b). Figure 4i shows that the FF method is the most effective method for calculating PVDR biologically, although with values found to be lower than expected for both doses and outside experiment error. This has been seen in previous studies attempting to analyse BPVDR in MRT using γH2AX assays[39].

It is also important to note that Fig. 4 calculates biological PVDR using the DSBER ratios taken from the average across samples, meaning that Eq. 3 computed the ratios of peak averages and valley averages. However, as Fig. 5 shows, the FF values can greatly vary for each sample image peak and valley. Each image clearly has a unique BPVDR value based on the cell response and spatial distribution at that given moment and slice of an MRT peak, regardless of dose (Fig. 5b-c). As the ratio of averages is not mathematically equal to the average of ratios, it becomes important to first calculate BPVDR for each image individually, as per Fig. 5a. Averaging these values yields far more accurate results in Fig. 5d.

Given PVDR is 8.9, the results in Fig. 5d agree exceptionally well with the BPVDR values obtained. Regardless of dose, both BPVDR values are well within error and very close to the expected physical value. By contrast, none of the other methods can produce a value close to 8.9. A student's statistical t-test used to obtain p value for BPVDR relative to the physical PVDR in Fig. 5 yields p > 0.9 for both doses in Fig. 5d using the FF Model. All other methods yield p < 0.001, indicating that conventional methods produce BPVDR results that a significantly statistically different from the expected physical value.

Whilst other authors have attempted to obtain BPVDR values with varying degrees of success with cells, or with tissues samples, some have concluded that using the foci/cell counting method, accurately determining BPVDR values is not possible[39,40]. However, in this study, Fig. 5 demonstrates that BPVDR can be simply and accurately found using the FF Model.

Additionally, Rothkamm et al. 2012 noted in their attempts to obtain BPVDR that the foci/cell method yielded values that were slightly lower than the expected PVDR values, explaining this as potentially due to the movement of cells in culture that may distort radiation geometry[39]. This potentially occurred in this study, where the BPVDR values were close to the actual PVDR value but slightly lower for radiation only MRT. However, both were still well within experimental error of the physical 8.9.

Likewise, when using foci intensity, Fig. 3d demonstrates peak intensities for γH2AX only reach several times that of their corresponding valleys. When comparing to the physically measured dose across the 400 μm pitch of a single microbeam, PVDR yields 8.9 (peak centre over average valley), yet the biological valley is notably higher. This further confirms that foci intensity alone is not sufficient to accurately quantify DSBs in peaks and valleys. As seen with Fig. 5d, only the FF Model yields accurate results that produce accurate BPVDR values.
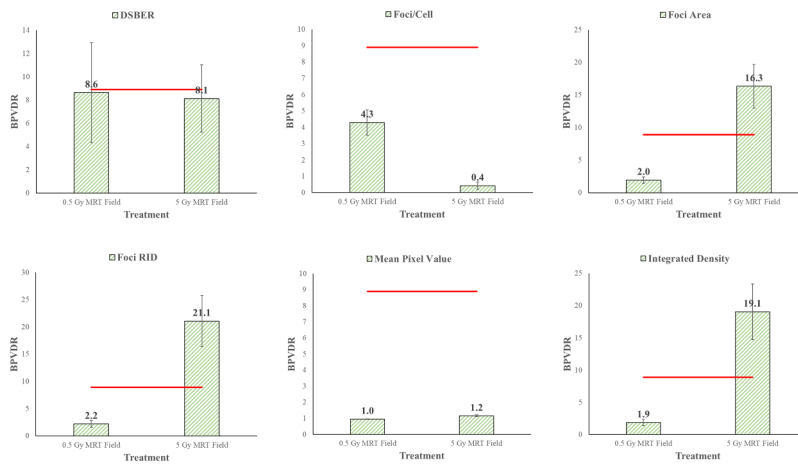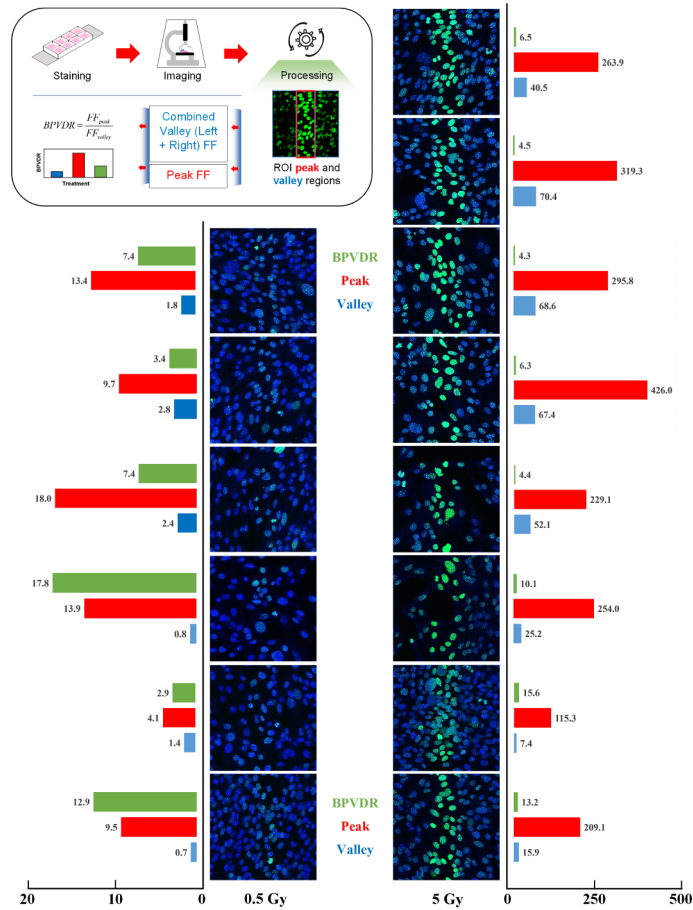
These observations were made prior to quantifying peaks and valleys in Figs. 4 and 5, and the ROI's accounted for this when determining FF values in peaks and valleys. As such, the BPVDR values in Fig. 5 consider the real valley DSB induction, and the real peak, to produce accurate BPVDR results. This is further verified by validating the accuracy of this method on a different cell line (Extended Data Fig. 1). Even using a different MRT valley dose and a differing microscope technique still produces an accurate BPVDR value that matches the physical PVDR, and hence reliable DSBER values are obtained using the FF method (see Supplementary Information). Evidently, this method then allows for meaningful use of foci intensity to provide a deeper bio-dosimetric analysis of MRT, whilst still providing data for use in the FF method to accurately quantify DSB enhancement, including the biological equivalent (as expressed in γH2AX markers) to physical PVDR.

◄**Fig. 5**. Foci Factor (FF) Model permits reliable biological PVDR (BPVDR) quantification from γH2AX MRT field images. (**a**), Method overview for acquiring and quantifying γH2AX images of MRT fields at various doses to obtain a bio-dosimetric PVDR measure. Methodology follows the framework displayed in Fig. 1 using the FF Model, whereby following staining and imaging, regions of interest are used over peaks and valleys to quantify DSBs. A BPVDR value is then obtained for each unique image with its respective peaks and valleys first prior to averaging. (**b-c**), Panels of 0.5 Gy and 5 Gy MRT (respectively) 93x images acquired by confocal microscopy and quantified to obtain a unique BPVDR result for each image sample. Quantification results are displayed as horizontal bar graphs either side of each image column, with DSBER results for each respective image peak (red) and valley (blue), as well as the unique PBVDR for that image (green). (**d-i**), Biological PVDR (BPVDR) graphs expressed as the ratio of the peak quantified values over the corresponding valley found for each method respectively from each unique image (**b-c**). Each BPVDR value is determined, for each method (DSBER via FF (**d**), foci/cell (**e**), area (**f**), RID (**g**), intensity (**h**) and integrated density (**i**)), as the quantification value of the peak over that of the corresponding valley for the same image. Each unique BPVDR for each image is then averaged for each separate method. A red line on each graph indicates the physical PVDR of 8.9, as physically measured by radiation detectors. All data points displayed in this figure represent the average of at least six quantified images across independent experimental trials ($n=6$) and display error bars representing standard error of the mean (SEM). Each sample imaged was fixed at 20 min post-irradiation.

Discussion

The broad use of γH2AX assays generally across disciplines due to its high sensitivity and specificity makes this immunofluorescent assay a reliable and flexible technique for DSB analysis. Whilst foci counting per cell nucleus is the common and trusted method of γH2AX image quantification[10,11], the limitations faced with this method still present a challenge to flexible use in many cases. Differences across each individual γH2AX focus even within the same image and cell nucleus can contribute to inaccuracies in counting methods, necessitating consideration of additional distinguishing criteria or image processing methodologies.

The most common metrics to quantify DSBs using the γH2AX assay are the number of γH2AX foci per cell, or the fluorescence intensity of these foci in cell populations[10,11]. However, many authors note higher densities of nuclear foci result in overlap that can reduce foci counting accuracy, causing underestimations of DSBs due to lack of separation[13,19]. Some studies recognise that whilst nuclear foci counting remains the standard quantification method, further analysis reveals the importance of additional factors and criteria for consideration, including foci size[14,15,17].

Foci size in images can vary greatly across 2D images and 3D z-stacks, as can the integrated pixel intensity in a single focus. Image noise, fluorescing debris, particulates, and additional signals beyond cell nuclei of a γH2AX image can skew foci counting, and often require processing methods to filter and consider foci by sizes and intensities in additional to noise filtration[11,17]. This study has carefully applied this logic to ensure reliable foci data are included in the quantification process, resulting in more accurate bio-dosimetric quantification via the FF method.

We have demonstrated that foci saturation in highly DNA-damaging conditions can result in significant overlap that can be difficult to resolve for its constituent foci. Foci area greatly increases in these cases[14], resulting in large foci clusters across radiation modalities with NPs present in 9LGS cells[4], and with cells expressing overwhelming DSB numbers in MRT peaks[40]. The average foci area and RID is observed to significantly increase, whilst foci/cell counts decrease as multiple foci merge into singular large foci. The FF method can consider all these factors simultaneously and hence overcome these limitations, yielding a DSBER value that more coherently matches the image being quantified. Furthermore, the use of the FF method across multiple radiation modalities and doses, and with and without NPs, attests to its broad and flexible potential for use across fields. This flexibility enhances the overall value of this method as it will allow for wider use across many disciplines using the γH2AX assay where quantification is desired.

Bio-dosimetric verification of the biological response to radiation has also been a challenge, notably for MRT[39,40]. Whilst physical PVDR has long been reliably measurable, biological measurement has been challenging using conventional foci counting methods. The capabilities of the microscope used for imaging will also affect foci counting and contribute to foci overlap and saturation, resulting in BPVDR quantification from γH2AX assays not being possible[40]. Other studies assessing the effect of NPs with RT modalities on glioma cells have used confocal microscopy for this reason[47]. Our study demonstrates the importance of high-resolution imaging using highly sensitive assays like γH2AX[19], and advanced techniques such as confocal microscopy to ensure reliable bio-dosimetry via these assays[39].

Additionally, we demonstrate our FF method is the only technique that can accurately quantify γH2AX images to confirm physical PVDR (Fig. 5d). All conventional methods yield statistically significantly different BPVDR values compared to the expected, whilst DSBER via the FF method matches precisely and well within experimental error across multiple MRT doses. This validation compared with a known, dosimetrically measurable quantity, one that has historically been challenging to confirm biologically, demonstrates the value of this method in overcoming both methodological and experimental limitations of γH2AX image quantification across various disciplinary fields[16,39,40].

A limitation of this method is that great consistency in sample staining and image acquisition is required to yield reliable results and mitigate the risk of outlier values. Additionally, identifying reasonable foci size and intensity limits for gating and filtration of foci, and applying these homogenously across processed image datasets, is essential in ensuring that legitimate foci can be sorted from background noise when counted. Another limitation of note when using the γH2AX assay is that ruptured cells may occur regardless of treatment or

condition, which is characterised heavy foci saturation and may skew the final analysis. Despite this possibility, a larger sample size over which to average can reduce this impact of this limitation. We believe all these limitations are generally not major concerns as these consistencies can be assured and reliability improved through rigorous application and repetition of the experimental method, and use of high-resolution microscopes for high quality imaging. Furthermore, the simple nature of the FF method will allow for automation via coding software for computational accuracy and efficiency, where such automated image analysis through computational approaches are already used with the γH2AX assay[11,17].

Overall, we propose our novel FF method will be valuable in many varied disciplines using γH2AX assays for DNA damage analysis. The versatile and simple nature of this model allows various forms of analysis, including use in bio-dosimetry. Our model's flexible use can also assist in overcoming limitations in traditional foci counting methods and provide reliable quantification in cases where conventional methods may not be sufficient, permitting further avenues of analysis with these assays.

Methods

Subculture of adherent cells

9 L gliosarcoma (9LGS) cells, obtained from the European Collection of Authenticated Cell Cultures (ECACC), were cultured in T75 cm^2 flasks (Greiner Bio-One via Interpath, AUS, #658175) containing complete Dulbecco's Modified Eagle Medium (c-DMEM) (Gibco, AUS, #11965118), with added 10% foetal bovine serum (FBS) (Gibco, AUS, #10099141), and 1% PenStrep (penicillin (10,000 units/mL) and streptomycin (10,000 μg/mL), supplied by Gibco, AUS, #15140122). Cultures were incubated at 37 °C and 5% (v/v) CO$_2$ and all 9LGS cells were grown with a doubling time of 36 h.

When passaged or harvested, cells are washed with 1x DPBS (Dulbecco's Phosphate Buffered Saline) (Ca^{2+} / Mg^{2+} free, Gibco, AUS, #14190144) before being suspended with 0.05% Trypsin EDTA (Gibco, AUS, #25300054). 9LGS cells were harvested via this passaging method, and counted and seeded for monolayers at 100% confluence into 1 cm^2 (well area) micro-chamber slide (Ibidi via DKSH, Germany, #80826) wells.

All 9LGS cell samples in slide wells were irradiated at confluence using a conventional broadbeam (CBB) X-rays at kilovoltage peak (kVp) energies using an orthovoltage device prior to γH2AX immunofluorescence staining. These were compared to 9LGS cells stained at the same time without radiation (0 Gy), and also to cells irradiated with synchrotron broadbeam (SBB) X-rays and synchrotron Microbeam Radiation Therapy (MRT) X-rays at comparable mean (keV) energies (albeit hundreds or even thousands of times higher dose rates) to the orthovoltage device.

Nanoparticle preparation

Thulium(III) oxide (Tm$_2$O$_3$) nanoparticles (99.9% trace metals basis) were obtained from Sigma Aldrich (via Merck, AUS, #289167). The Tm$_2$O$_3$ NPs (TmNPs) were sonicated for 40 min in DPBS (Ca^{2+} / Mg^{2+} free, Gibco, AUS, #14190144) at a concentration of 1 mg/mL (w/v), to separate particles using an ultrasonic water bath (Branson). Following the protocol of Engels et al. 2018[4], the NPs were then added to samples for an optimal concentration of 20 μg/cm^2 on the surface of the slide wells 24 h priors to the cells reaching 100% confluence.

Cell irradiation with a conventional orthovoltage radiation device

Irradiation of 9LGS cells by conventional boradbeam (CBB) X-rays was performed at Prince of Wales Hospital, Randwick, NSW, Australia, following the irradiation protocol of Oktaria et al. 2015 and Engels et al., 2018[4,29,48]. Using a Nucletron Oldelft Therapax DXT 300 Series 3 Orthovoltage unit (Nucletron B.V., Veenendaal, The Netherlands)[4,29,48], this 150 kVp kilovoltage peak energy (66 keV mean energy)[4,29] was chosen to target the maximum mass energy absorption of thulium oxide relative to water, as chosen by Engels et al., 2018[4].

A monolayer of 9LGS cells was used in micro-chamber slides for irradiation, all under 8 mm of complete DMEM culture media and Hanks Balanced Salt Solution (HBSS with phenol red (Gibco, AUS), #24020-117). All slides were irradiated horizontally at 50 cm from the source in full scatter conditions, including solid water adjacent to each side of the slides[4,29,48], with all samples falling entirely within the radiation field. X-rays were generated at the chosen energy with a beam current of 20 mA using an inherent filtration of 3 mm Be, and additional 0.35 mm of copper and 1.5 mm of aluminium (HVL = 0.68 mm Cu). These x-rays were used to irradiate the cells with a dose rate of 0.75 Gy min^{-1} at depth[4,29].

Synchrotron radiation beam configurations, parameters and dosimetry for broadbeams and microbeams

Irradiation of cell samples was conducted in the Imaging and Medical Beamline (IMBL) of the Australian Synchrotron, Melbourne, Australia, using the dynamic option of IMBL's hutch 2B.

The synchrotron wiggler field was chosen to be 2 T with a Cu/Al filtration (69 keV mean energy) for SBB and MRT for comparable energy to CBB, yet at far higher dose rates. For MRT fields, the ratio defining the escalation in dose delivered into the peak regions where the X-ray microbeams are incident upon the cells, D$_{peak}$ (Gy), to the dose delivered by the MRT field into the valley spacings between the beam tracks, D$_{valley}$ (Gy), is defined the Peak-to-Valley Dose Ratio (PVDR)[49,50], as shown in Eq. 4.

$$PVDR = \frac{D_{peak}}{D_{valley}} \tag{4}$$

The microbeams were produced by passing the synchrotron beam a tungsten carbide multi-slit collimator (MSC) 8 mm thick, 40 mm wide and 4 mm high, as described by Stevenson et al., 2017[51]. This produced an array of 25

microbeams at 50 μm width and 400 μm pitch. The intrinsic field size of 10 mm x 60 mm (width x height) used for both SBB and MRT necessitated the use of two columns to irradiate the imaging micro slides.

Complete details for beam configuration parameters can be found in Table 1 and further in Dipuglia et al. 2019 and Davis et al. 2021[52,53]. For dosimetry, for both SBB and MRT at the IMBL of the Australian Synchrotron, we use a PinPoint ionization chamber (PTW 31014, Freiburg, Germany) calibrated to a traceable standard, and an RMI-457 Gammex Solid Water* phantom (Gammex-RMI, Middleton, WI, USA)[54]. We further use an X-Tream dosimetry system using an epitaxial silicon detector (with micron-scale spatial resolution)[55,56] calibrated at reference conditions of a 20×20 mm^2 SBB field at 20 mm depth, a PTW microdiamond[57,58], and Gafchromic* EBT3 film. Complete details of this protocol can be found in Engels et al. 2020[33].

Prior to each experiment, final *in vitro* doses were verified at the same depth where the monolayer of cells is located (24 mm) on custom-built Gammex Solid Water* phantom to hold the cell microslide at a 30° incline (to allow full exposure of all cells without leakage of internal contents from the micro-chamber slide). Solid water is placed adjacent to the sides of the slide and on top to simulate a 24 mm depth in water. Each slide well was pre-filled with HBSS (with phenol red (Gibco, AUS)) to the top to ensure a complete water-based environment prior to irradiation. A Gafchromic* EBT3 film was placed on the back-side of each cell micro-chamber slide to confirm the irradiation geometry (for both SBB and MRT).

Materials for staining of cells for γ-H2AX immunofluorescence imaging

The materials for the immunofluorescent staining of 9LGS cells in micro-chamber slides included several consumable materials, chemicals, and devices. Following treatment, cell samples adhered in slides, micro-pipettes and tips, pipette guns, conical tubes and tube racks, were required. Ice buckets were used for cooling (to ice-cold temperatures of 4°C) of chemicals and slides following radiation, and an electric rocker was used samples being washed and blocked.

100% methanol (Sigma Aldrich, AUS, #34860) at 4°C (in ice buckets) was used as the fixative and permeabilization agent. Bovine Serum Albumin (BSA) (Sigma Aldrich, AUS, #A9418) was diluted at 3% (w/v) in DPBS (salt free) for use as a blocking buffer solution (BSA-PBS).

DPBS (salt free) was used throughout as a washing solution between steps, or as a dilution solution for BSA-PBS blocking buffer. BSA-PBS was then used as a dilution solution for a primary and a secondary antibody.

Mouse anti-phospho-Histone H2A.X (Ser139), clone JBW301 (Merck Millipore, AUS, #05-636) was used as the primary γ-H2AX antibody for specific binding to Double-strand DNA breaks (DSBs) sites within cell nuclei. A secondary antibody Goat anti-Mouse IgG1 Cross-Absorbed, Alexa Fluor 488 (Invitrogen, AUS, #A21121) was used to bind to the primary antibody at DSB sites, delivering conjugated fluorophore Alex Fluor 488 to the site for visual detection by a confocal microscope.

A Hoechst 33342 nuclear stain (Sigma-Aldrich via Merck, AUS, #14533) was used as a counterstain for nuclear DNA to reveal the nucleus when imaging. A layer of DPBS was left in each well prior to addition of the Hoechst stain.

Method for γ-H2AX immunofluorescence staining

Double-strand breaks were visually revealed via γ-H2AX detection and imaging by confocal microscopy[4,10,11]. Images were quantified by subsequent analysis with ImageJ. Microscopy was performed for a monolayer of 9LGS cultured for confluence of 100,000 cells in the wells of an 8-well micro-chamber slide in accordance with above methods. Different wells were seeded for each treatment, and at confluence of 100%, cells were irradiated in accordance with above parameters.

At 20 min following irradiation, cells were washed twice with ice-cold DPBS per well before fixation with ice-cold 100% methanol per well for 20 min. Wells were then each washed three times with cold DPBS for 5 min at room temperature. Following this, the chambers are treated twice with a blocking buffer solution of 3% bovine serum albumin (BSA) in BPS for 15 min at room temperature. A primary antibody (Mouse anti-phospho-Histone H2A.X (Ser139), clone JBW301) was added 1:500 in 3% BSA-DPBS for a concentration of 2 μg/mL to the cells (200 ng per 1×10^5 cells), which were incubated for 2 h at room temperature.

Following incubation, the cells were washed three times with DPBS for 5 min at room temperature. A secondary antibody (Goat anti-Mouse IgG1 Cross-Absorbed, Alexa Fluor 488) was added 1:500 in 3% BSA-PBS for a concentration of 4 μg/mL to the cells (200 ng per 1×10^5 cells) and incubated at room temperature for 1

Mode	Wiggler Field (T)	Inherent Filtration (mm)	Mean Energy (keV)	Beam height (mm); Beam, width (cm); Number of columns	Intrinsic dose rate (Gy/s) in Solid water	PVDR
CBB	N/A	Be (3.00) Cu (0.35) Al (1.50)	66	N/A	0.0125 at 8 mm depth in c-DMEM	N/A
SBB	2	Cu (1.41) Al (2.82)	69	0.500; 0.140; 4	74.1 at 24 mm depth in Solid Water	N/A
MRT	2	Cu (1.41) Al (2.82)	69	0.480; 0.385; 4	50.3 (peak), 5.7 (valley) at 24 mm depth	8.9

Table 1. Dosimetric parameters and beam configurations for SBB and MRT used at the Australian Synchrotron IMBL. All beam geometry and intrinsic dose rates are measured at the sample position. CBB configuration parameters are shown as described for comparison to the low dose rate radiation therapy modality.

h in darkness. Finally, cells were again washed twice with 300 μL of DPBS before 100 μL of DPBS was added to each well. 2 μL of 1 mg/mL Hoechst 33342 was then added to each well for 20 min at room temperature (2 μg per 1×10^5 cells), before cells were imaged with a Leica TCS SP8 confocal microscope (Leica Microscope Systems, AUS) with a 93x glycerol objective at room temperature.

The confocal microscope utilised a laser providing a 488 nm excitation with a detection range for the Alex Fluor 488 fluorophore (FITC), and another 405 nm laser providing with the range for the Hoechst 33342 nuclear counterstain (DAPI). Detection ranges were set to a minimum 10 nm above the excitation wavelengths for each laser and higher. The voltage gains were optimised using the images which had the most intense γ-H2AX foci signals to avoid saturation. Sequential imaging of separate channels (optical bright field, DAPI, FITC) was used for 512×512 pixel images to avoid cross-talk of signal detection from different laser excitations. A 2×2 tile scan with a z-stack of 10 slices (1.2 μm thickness) was taken per image, resulting in images greater than 200 μm x 200 μm at 93x resolution to include sufficient cells (around 50–100 cells per image). At least 3 images were taken per well. Additionally, 20x resolution images are also taken to capture multiple peaks in one image, and further avoid overexposure of fluorophores that may result in photo-bleaching at higher resolutions with tile scans. These images were all then analysed via the Leica LasX Application Suite (Leica Microscope Systems), ImageJ (1.53k)[44], and Microsoft Excel (2016).

Image processing method for quantification of γ-H2AX confocal images

The Z-stack images were exported as TIF files (separated by channel) from the Leica LasX Application Suite for processing on ImageJ (v1.53k). Foci quantification was performed on the full 3D stack of the 488 nm channel for γ-H2AX, and cell counting was performed on the 405 nm channel stack for Hoechst 33342 nuclei detection.

Foci quantification via ImageJ on the 488 nm channel first required thresholding of images to a minimum pixel value of 35 (to max 255)[44] to exclude background noise.

The Analyze Particles tool was then used, with minimum particle size (foci area) for count set at 0.01 μm² (to maximum size infinity) and circularity 0.00–1.00 and the process was applied to all individual slices within the foci Z-stack. These numbers were chosen to capture all reasonable data possible from potential foci, as a later filter would be applied to discount background noise. The data from the particle analysis of foci, showing foci area, mean foci pixel value, integrated density (IntDen) (mean value multiplied by area) and raw integrated density (RawIntDen) (sum of all pixel values in the foci)[44], was exported to an Excel spreadsheet for computation.

This process was repeated for all images. The total number of particles detected is related to the foci number, the area provides the foci size, whilst mean pixel value and RawIntDen relate to foci intensity. These foci characteristics are related to the DSBs expression.

For cell counting, the entire 405 nm channel image sequence was processed with a 3D maximum intensity Z-projection to collapse all slices into a single image slice. The Despeckle tool was used to remove background noise, followed by a Gaussian Blur filter (sigma radius 3; no scaled units) to blur the nuclei into singular objects. A threshold was then applied (70 minimum to 255 maximum pixel value), followed by binarization of the image. The fill holes tool was then used to form the nuclei into an unbroken object, followed by use of the Watershed tool to separate close-situating nuclei from becoming a single object[44]. The Analyze Particles tool was then used to count cell nuclei. A minimum area of 50 μm² (to maximum infinity) was used as the particle size range (and circularity 0.00–1.00) before running the analysis. Once run, the total number of particles is equal to the total number of cells (via nuclei) in that image stack. This number was copied to the Excel spreadsheet with the foci count data for computation.

The total number of foci (and therefore DSBs) was divided by the number of cell nuclei counted in the same image to obtain DSBs per cell (using the model developed in the Results). This value was averaged and normalized for each treatment to that of the untreated control, which was used to indicate the overall increase in DSBs induced by said treatment.

Statistical analyses

All error bars were calculated as standard error of the mean (SEM) using 2 standard deviations (95% confidence interval) of the mean divided by square root of the number of images used. For each sample tested, at least 6 images drawn from at least 3 replicates (at least one triplicate of images was measured for each independently repeated sample) and at least 2 independent repeats were averaged to obtain means.

A Student's t-test was used to compare samples whose DSBER value distributions approximated the normal distribution, with the unpaired heteroscedastic t-test for independent samples. One-tailed tests were used when comparing to untreated controls as the increase was the primary interest, while all other cases used a two-tailed t-test. All compared data was unpaired arising for separate individual samples. The p values for each statistical test are presented in the corresponding figure legend.

Method consistency

Statistical reliability and consistency of the method were also affirmed by verification of results by alternative means. This included by assessment and validation of the method on a different cell lines under different conditions, and by multiple differing experimenters.

Individual trials of the experiment are displayed in some figures for comparison. A different cell line is assessed, the results for which are displayed in Supplementary Information. Different experimenters independently and successfully used the method to obtain the same results displayed (data not shown to prevent repeated display of results and figure repetition).

Reporting summary

Further information on research design is available in the Nature Portfolio Reporting Summary linked to this article.

Data availability

All data is available within this paper.

Code availability

All image analysis code functions are available via ImageJ from the National Institutes of Health,United States (https://imagej.nih.gov/ij/index.html). All computational functions for dataset analysisand calculations are available in Microsoft Excel from the Microsoft 365 software suite(https://www.microsoft.com/en-au/microsoft-365/excel). All were applied to image analysis inaccordance with the methods and protocols listed within this paper.

References

1. Kuo, L. J. & Yang, L. X. Gamma-H2AX - a novel biomarker for DNA double-strand breaks. *Vivo*. **22**, 305–309 (2008).
2. Abbas, Z. & Rehman, S. Neoplasm. *(ed Hafiz Naveed Shahzad) Ch*. **6**, 140–157 (2018). (IntechOpen.
3. Barnett, G. C. et al. Normal tissue reactions to radiotherapy: towards tailoring treatment dose by genotype. *Nat. Rev. Cancer*. **9**, 134–142. https://doi.org/10.1038/nrc2587 (2009).
4. Engels, E. et al. Thulium Oxide nanoparticles: a new candidate for image-guided radiotherapy. *Biomed. Phys. Eng. Expr*. **4** https://doi.org/10.1088/2057-1976/aaca01 (2018).
5. Gianfaldoni, S. et al. An overview on Radiotherapy: from its history to its current applications in Dermatology. *Open. Access. Maced J. Med. Sci*. **5**, 521–525. https://doi.org/10.3889/oamjms.2017.122 (2017).
6. Hossain, M. A., Lin, Y. & Yan, S. Single-strand Break End Resection in Genome Integrity: mechanism and regulation by APE2. *Int. J. Mol. Sci*. **19** https://doi.org/10.3390/ijms19082389 (2018).
7. Mahaney, B. L., Meek, K. & Lees-Miller, S. P. Repair of ionizing radiation-induced DNA double-strand breaks by non-homologous end-joining. *Biochem. J*. **417**, 639–650. https://doi.org/10.1042/BJ20080413 (2009).
8. Tubbs, A. & Nussenzweig, A. Endogenous DNA damage as a source of genomic instability in Cancer. *Cell* **168**, 644–656. https://doi.org/10.1016/j.cell.2017.01.002 (2017).
9. Vitor, A. C., Huertas, P., Legube, G. & de Almeida, S. F. Studying DNA double-strand break repair: an ever-growing Toolbox. *Front. Mol. Biosci*. **7**, 24. https://doi.org/10.3389/fmolb.2020.00024 (2020).
10. Ivashkevich, A., Redon, C. E., Nakamura, A. J., Martin, R. F. & Martin, O. A. Use of the gamma-H2AX assay to monitor DNA damage and repair in translational cancer research. *Cancer Lett*. **327**, 123–133. https://doi.org/10.1016/j.canlet.2011.12.025 (2012).
11. Ivashkevich, A. N. et al. gammaH2AX foci as a measure of DNA damage: a computational approach to automatic analysis. *Mutat. Res*. **711**, 49–60. https://doi.org/10.1016/j.mrfmmm.2010.12.015 (2011).
12. Borras, M., Armengol, G., De Cabo, M., Barquinero, J. F. & Barrios, L. Comparison of methods to quantify histone H2AX phosphorylation and its usefulness for prediction of radiosensitivity. *Int. J. Radiat. Biol*. **91**, 915–924. https://doi.org/10.3109/09553002.2015.1101501 (2015).
13. Lapytsko, A., Kollarovic, G., Ivanova, L., Studencka, M. & Schaber, J. FoCo: a simple and robust quantification algorithm of nuclear foci. *BMC Bioinform*. **16**, 392. https://doi.org/10.1186/s12859-015-0816-5 (2015).
14. Lee, U. S., Lee, D. H. & Kim, E. H. Characterization of gamma-H2AX foci formation under alpha particle and X-ray exposures for dose estimation. *Sci. Rep*. **12**, 3761. https://doi.org/10.1038/s41598-022-07653-y (2022).
15. Martin, O. A. et al. Statistical analysis of kinetics, distribution and co-localisation of DNA repair foci in irradiated cells: cell cycle effect and implications for prediction of radiosensitivity. *DNA Repair. (Amst)* **12**, 844–855. https://doi.org/10.1016/j.dnarep.2013.07.002 (2013).
16. Stenvall, A., Larsson, E., Holmqvist, B., Strand, S. E. & Jonsson, B. A. Quantitative gamma-H2AX immunofluorescence method for DNA double-strand break analysis in testis and liver after intravenous administration of (111)InCl(3). *EJNMMI Res*. **10**, 22. https://doi.org/10.1186/s13550-020-0604-8 (2020).
17. Cai, Z., Vallis, K. A. & Reilly, R. M. Computational analysis of the number, area and density of gamma-H2AX foci in breast cancer cells exposed to (111)In-DTPA-hEGF or gamma-rays using Image-J software. *Int. J. Radiat. Biol*. **85**, 262–271. https://doi.org/10.1080/09553000902748757 (2009).
18. Nair, S. et al. The impact of dose rate on DNA double-strand break formation and repair in human lymphocytes exposed to fast Neutron Irradiation. *Int. J. Mol. Sci*. **20** https://doi.org/10.3390/ijms20215350 (2019).
19. Reddig, A., Roggenbuck, D. & Reinhold, D. Comparison of different immunoassays for γH2AX quantification. *J. Lab. Precision Med*. **3**, 80–80. https://doi.org/10.21037/jlpm.2018.09.01 (2018).
20. Chen, F., Ehlerding, E. B. & Cai, W. Theranostic nanoparticles. *J. Nucl. Med*. **55**, 1919–1922. https://doi.org/10.2967/jnumed.114.146019 (2014).
21. Cheng, Y., Morshed, R. A., Auffinger, B., Tobias, A. L. & Lesniak, M. S. Multifunctional nanoparticles for brain tumor imaging and therapy. *Adv. Drug Deliv Rev*. **66**, 42–57. https://doi.org/10.1016/j.addr.2013.09.006 (2014).
22. Ediriwickrema, A. & Saltzman, W. M. Nanotherapy for Cancer: Targeting and Multifunctionality in the future of Cancer therapies. *ACS Biomater. Sci. Eng*. **1**, 64–78. https://doi.org/10.1021/ab500084g (2015).
23. Hainfeld, J. F., Dilmanian, F. A., Slatkin, D. N. & Smilowitz, H. M. Radiotherapy enhancement with gold nanoparticles. *J. Pharm. Pharmacol*. **60**, 977–985. https://doi.org/10.1211/jpp.60.8.0005 (2008).
24. Retif, P. et al. Nanoparticles for Radiation Therapy Enhancement: the key parameters. *Theranostics*. **5**, 1030–1044. https://doi.org/10.7150/thno.11642 (2015).
25. Engels, E., Lerch, M., Corde, S. & Tehei, M. Efficacy of 15 nm gold nanoparticles for image-guided Gliosarcoma Radiotherapy. *J. Nanotheranostics*. **4**, 480–495. https://doi.org/10.3390/jnt4040021 (2023).
26. Brown, R. et al. Nanostructures, concentrations and energies: an ideal equation to extend therapeutic efficiency on radioresistant 9L tumor cells using Ta2O5 ceramic nanostructured particles. *Biomed. Phys. Eng. Expr*. **3** https://doi.org/10.1088/2057-1976/aa56f2 (2017).
27. Engels, E. et al. Synchrotron activation radiotherapy: Effects of dose-rate and energy spectra to tantalum oxide nanoparticles selective tumour cell radiosensitization enhancement. *Journal of Physics: Conference Series* 777 1–4 (2016).
28. Engels, E. et al. Optimizing dose enhancement with Ta(2)O(5) nanoparticles for synchrotron microbeam activated radiation therapy. *Phys. Med*. **32**, 1852–1861. https://doi.org/10.1016/j.ejmp.2016.10.024 (2016).

29. McDonald, M. et al. Radiosensitisation enhancement effect of BrUdR and Ta2O5 NSPs in combination with 5-Fluorouracil antimetabolite in kilovoltage and megavoltage radiation. *Biomed. Phys. Eng. Expr*. **4** https://doi.org/10.1088/2057-1976/aabab2 (2018).

30. Engels, E. et al. Advances in modelling gold nanoparticle radiosensitization using new Geant4-DNA physics models. *Phys. Med. Biol*. **65**, 225017. https://doi.org/10.1088/1361-6560/abb7c2 (2020).

31. McKinnon, S. et al. Study of the effect of ceramic Ta(2)O(5) nanoparticle distribution on cellular dose enhancement in a kilovoltage photon field. *Phys. Med*. **32**, 1216–1224. https://doi.org/10.1016/j.ejmp.2016.09.006 (2016).

32. Vogel, S. et al. Fluorescent gold nanoparticles in suspension as an efficient Theranostic Agent for highly Radio-Resistant Cancer cells. *J. Nanotheranostics*. **4**, 37–54. https://doi.org/10.3390/jnt4010003 (2023).

33. Engels, E. et al. Toward personalized synchrotron microbeam radiation therapy. *Sci. Rep*. **10**, 8833. https://doi.org/10.1038/s41598-020-65729-z (2020).

34. Mazal, A. et al. FLASH and minibeams in radiation therapy: the effect of microstructures on time and space and their potential application to protontherapy. *Br. J. Radiol*. **93**, 20190807. https://doi.org/10.1259/bjr.20190807 (2020).

35. Montay-Gruel, P., Corde, S. & Laissue, J. A. Bazalova-Carter, M. FLASH radiotherapy with photon beams. *Med. Phys*. **49**, 2055–2067. https://doi.org/10.1002/mp.15222 (2022).

36. Mukumoto, N. et al. Sparing of tissue by using micro-slit-beam radiation therapy reduces neurotoxicity compared with broad-beam radiation therapy. *J. Radiat. Res*. **58**, 17–23. https://doi.org/10.1093/jrr/rrw065 (2017).

37. Slatkin, D. N., Spanne, P., Dilmanian, F. A., Gebbers, J. O. & Laissue, J. A. Subacute neuropathological effects of microplanar beams of x-rays from a synchrotron wiggler. *Proc. Natl. Acad. Sci. U S A*. **92**, 8783–8787. https://doi.org/10.1073/pnas.92.19.8783 (1995).

38. Schultke, E. et al. Microbeam radiation therapy - grid therapy and beyond: a clinical perspective. *Br. J. Radiol*. **90**, 20170073. https://doi.org/10.1259/bjr.20170073 (2017).

39. Rothkamm, K. et al. In situ biological dose mapping estimates the radiation burden delivered to 'spared' tissue between synchrotron X-ray microbeam radiotherapy tracks. *PLoS One* **7**, e29853. https://doi.org/10.1371/journal.pone.0029853 (2012).

40. Ventura, J. A. et al. The γH2AX DSB marker may not be a suitable biodosimeter to measure the biological MRT valley dose,. *International Journal of Radiation Biology* 97, 642–656, doi:0.1080/09553002.1893854 (2021). (2021).

41. Vozenin, M.-C., Hendry, J. H. & Limoli, C. L. Biological benefits of Ultra-high Dose Rate FLASH Radiotherapy: sleeping Beauty Awoken. *Clin. Oncol. (R Coll. Radiol)*. **31**, 407–415. https://doi.org/10.1016/j.clon.2019.04.001 (2019).

42. Wang, X., Luo, H., Zheng, X. & Ge, H. FLASH radiotherapy: research process from basic experimentation to clinical application. *Precision Radiation Oncol*. **5**, 259–266. https://doi.org/10.1002/pro6.1140 (2021).

43. Wilson, J. D., Hammond, E. M., Higgins, G. S. & Petersson, K. Ultra-high Dose Rate (FLASH) Radiotherapy: silver bullet or Fool's gold? *Front. Oncol*. **9**, 1563. https://doi.org/10.3389/fonc.2019.01563 (2019).

44. Schneider, C. A., Rasband, W. S. & Eliceiri, K. W. NIH Image to ImageJ: 25 years of image analysis. *Nat. Methods*. **9**, 671–675. https://doi.org/10.1038/nmeth.2089 (2012).

45. Davis, C. K. & Vemuganti, R. DNA damage and repair following traumatic brain injury. *Neurobiol. Dis*. **147**, 105143. https://doi.org/10.1016/j.nbd.2020.105143 (2021).

46. Gartner, A. & Engebrecht, J. DNA repair, recombination, and damage signaling. *Genetics*. **220** https://doi.org/10.1093/genetics/iyab178 (2022).

47. Stefancikova, L. et al. Effect of gadolinium-based nanoparticles on nuclear DNA damage and repair in glioblastoma tumor cells. *J. Nanobiotechnol*. **14** https://doi.org/10.1186/s12951-016-0215-8 (2016).

48. Oktaria, S. et al. Indirect radio-chemo-beta therapy: a targeted approach to increase biological efficiency of x-rays based on energy. *Phys. Med. Biol*. **60**, 7847–7859. https://doi.org/10.1088/0031-9155/60/20/7847 (2015).

49. Annabell, N., Yagi, N., Umetani, K., Wong, C. & Geso, M. Evaluating the peak-to-valley dose ratio of synchrotron microbeams using PRESAGE fluorescence. *J. Synchrotron Radiat*. **19**, 332–339. https://doi.org/10.1107/S0909049512005237 (2012).

50. Lerch, M. L. F. et al. Dosimetry of intensive synchrotron microbeams. *Radiat. Meas*. **46**, 1560–1565. https://doi.org/10.1016/j.radmeas.2011.08.009 (2011).

51. Stevenson, A. W. et al. Quantitative characterization of the X-ray beam at the Australian Synchrotron Imaging and Medical Beamline (IMBL). *J. Synchrotron Radiat*. **24**, 110–141. https://doi.org/10.1107/S1600577516015563 (2017).

52. Davis, J. A. et al. X-TREAM protocol for microbeam radiation therapy at the Australian Synchrotron. *J. Appl. Phys*. **129** https://doi.org/10.1063/5.0040013 (2021).

53. Dipuglia, A. et al. Validation of a Monte Carlo simulation for Microbeam Radiation Therapy on the imaging and medical beamline at the Australian Synchrotron. *Sci. Rep*. **9**, 17696. https://doi.org/10.1038/s41598-019-53991-9 (2019).

54. Cameron, M. et al. Comparison of phantom materials for use in quality assurance of microbeam radiation therapy. *J. Synchrotron Radiat*. **24**, 866–876. https://doi.org/10.1107/S1600577517005641 (2017).

55. Fournier, P. et al. X-Tream dosimetry of highly brilliant X-ray microbeams in the MRT hutch of the Australian Synchrotron. *Radiat. Meas*. **106**, 405–411. https://doi.org/10.1016/j.radmeas.2017.01.011 (2017).

56. Petasecca, M. et al. X-Tream: a novel dosimetry system for Synchrotron Microbeam Radiation Therapy. *J. Instrum*. **7**, 1–15. https://doi.org/10.1088/1748-0221/7/07/P07022 (2012).

57. Davis, J. A. et al. X-Tream dosimetry of synchrotron radiation with the PTW microDiamond. *J. Instrum*. **14**, P10037–P10037. https://doi.org/10.1088/1748-0221/14/10/p10037 (2019).

58. Dukes, J. D., Whitley, P. & Chalmers, A. D. The MDCK variety pack: choosing the right strain. *BMC Cell. Biol*. **12**, 43. https://doi.org/10.1186/1471-2121-12-43 (2011).

Acknowledgements

Author contributions

M.V., S.V., E.E. and M.T. conceived the study. M.V. and S.V. oversaw experimental design. M.V., S.V. and E.E. developed the conceptual model and framework. M.V. identified the treatment conditions and immortalised cell lines for testing and validation. M.V. prepared all cell lines, nanoparticles, and experimental materials. M.V., S.V., C.H., A.K., A.O.K., D.P. and M.T. performed cell sample staining. M.V. performed all stained sample microscopy, and all image processing and analysis. M.V. performed all dataset filtering, quantification computations, and statistical and graphical analyses. J.P., M.B., M.C., M.L. and S.C. performed the radiation dosimetry and operated all radiation devices and facilities used. M.V. wrote the manuscript with a significant contribution from

Declarations

Competing interests
The authors declare no competing interests.

Additional information
Supplementary Information The online version contains supplementary material available at https://doi.org/10.1038/s41598-024-76683-5.

Correspondence and requests for materials should be addressed to M.T.

Reprints and permissions information is available at www.nature.com/reprints.

Publisher's note Springer Nature remains neutral with regard to jurisdictional claims in published maps and institutional affiliations.